Marangoni-driven pattern formation in an absorbing binary mixture

PF. Arroiabe,[1] M. Martinez-Agirre,[1] A. Nepomnyashchy,[2] M. M. Bou-Ali,[1] and V. Shevtsova[1,3]
[1)]*Fluid Mechanics Group, Faculty of Engineering, Mondragon University, 20500 Mondragon, Spain*
[2)]*2Department of Mathematics, Technion–Israel Institute of Technology, 32000 Haifa, Israel*
[3)]*IKERBASQUE, Basque Foundation for Science, Plaza Euskadi 5, 48009 Bilbao, Spain*

(*Electronic mail: x.vshevtsova@mondragon.edu)

(Dated: 25 September 2024)

We investigate the evolution of convective instability in a LiBr-water binary mixture, driven by thermal and solutal Marangoni stresses, through numerical simulations. A small perturbation in absorption at the surface disturbs the equilibrium, generating surface tension gradients that drive Marangoni flows. To isolate and better understand the interplay between the Marangoni effect and absorption, we extended the previous study by investigating the LiBr-water binary system in the absence of gravity. For the first time, we observed the formation of a stable rim in an absorbing binary mixture, which underwent a slight contraction followed by rapid Marangoni spreading. This behaviour shows similarities with the flow patterns seen in the 'coffee-ring' and Marangoni spreading phenomena in evaporating binary mixtures. On the subsurface, convective motion breaks into several vortices, accompanied by the formation of plumes with reduced mass fraction. As the system evolves, the symmetry of the flow pattern around the cell center breaks down. The absence of buoyancy-driven forces eliminates a key counterforce to Marangoni flows, transforming the previously ordered patterns into non-periodic oscillations, followed by the development of non-stationary but regular patterns. These results complement our earlier findings [PF. Arroiabe et al., Phys. Fluids 022119 (2024)[1]], where gravitational forces obscured these phenomena.

I. INTRODUCTION

Absorption technology attracts significant attention due to its potential for sustainable and energy-efficient heating and cooling[2]. A critical component of absorption machines is the absorber, due to its low heat and mass transfer coefficients, significantly impacting the overall performance of the system. Understanding the heat and mass transfer processes within the absorber is crucial for improving the efficiency of absorption machines[3,4]. While our attention in this study is focused on absorption chillers, where the LiBr solution absorbs water vapour to facilitate cooling, some similarity in the overarching principles of mass transfer, diffusion and interfacial phenomena can be found with pollutant absorption systems used in air and liquid purification, where absorbents capture pollutants[5,6].

When an initially quiescent fluid experiences non-uniform absorption at its free surface, the surface tension of the fluid varies with concentration and temperature. This variation creates a shear stress that drags fluid along the interface towards regions of higher surface tension, a phenomenon known as Marangoni flow. Since the 1990s, the concept of using Marangoni convection to enhance heat and mass transfer on an absorbing interface has gained considerable attention[7–11]. In order to understand the role of the Marangoni effect, numerous experimental studies have been conducted in small-scale stagnant pools with the addition of various surfactants to increase the capillary force[9,12–14]. In simulations with realistic LiBr–water solution parameters, the presence of surfactant was modelled by adjusting the value of the surface tension gradient with the mass fraction. However, a comparison of the numerical predictions with the experimental results revealed a significant discrepancy, indicating that the numerical models were not exact[7,9,10]. There was then a decade-long pause in modeling convection in stagnant pools with an absorbing interface.

A deeper insight in the absorption dynamics in the presence of buoyant and Marangoni convection, without the addition of surfactant, has been provided in our recent paper[1]. The flow emerging from local interface perturbation was categorized in three regimes developing in successive time intervals. In the first regime, noticeable changes in flow velocity (V), mass fraction (w), and temperature (T) occur exclusively in the central part of the cell, where variations in surface tension have a dominant influence. The second regime is characterized by a significant and abrupt changes in w, T, and V, due to the onset of buoyant convection. The third regime is distinguished by the emergence of ordered patterns in all quantities, with periodicity evident in both space and time.

These results clearly demonstrated that in the dynamics of absorption and heat mass transfer, the buoyancy force plays an important role. To isolate and further elucidate the interplay between the Marangoni effect and absorption, we extended the previous study by placing the LiBr-water binary system under microgravity conditions ($g = 0$). The behavior of the system with and without gravity is surprisingly different. When $g = 0$, we observe for the first time the occurrence of a stable rim in an absorbing binary mixture, where the flow pattern has similarity with the well-known "coffee-ring" phenomenon in evaporating liquids[15–17]. Furthermore, we observe a small retraction of this rim, followed by rapid Marangoni spreading at a later stage which is also the subject of numerous studies[18–20]. In such studies, the Marangoni effect usually involves both thermal and solutal convection. The variety of patterns that emerge has been experimentally studied in binary mixtures, where both types of convection

are present, but solutal convection is driven by the Soret effect[21,22]. It was reported that evaporation primarily influenced pattern formation during the early stages, while the Soret effect became more significant later[21]. Our LiBr-water system also exhibits the Soret effect, and similar to the NaCl-water mixture, it has a negative Soret coefficient at the composition of interest[23]. This opens up further opportunities for research.

We should note that absorption is very different from evaporation since, in absorption, the temperature and concentration at the interface are continuously related by equilibrium conditions[24,25]:

$$w_e(T,P_0) = w^*_{e0} + w^*_T(T-T_0) \tag{1}$$

where w^*_{e0} is the equilibrium concentration at the reference state, and $w^*_T = \partial w/\partial T$ is the linear concentration coefficient, both depend on pressure.

II. PROBLEM FORMULATION

This study examines convective instability in a LiBr-water binary mixture that absorbs water vapor. Although LiBr dissociates in water, it is treated as a single component in this investigation. This approach is justified by considering the macroscopic motion of the LiBr solution as a whole, characterized by macroscopic quantities measured for this solution. Local equilibrium between the concentrations of ions with opposite electrical charges is maintained by the condition of zero macroscopic bulk charge density. Since the study does not involve an electric field, thermoelectric phenomena, or other processes where the ionic charge is significant, using the standard macroscopic equations for binary solutions, typically applied in the literature for salt solutions, is justified. Therefore, it is sufficient to use a single variable (w) for the solute mass fraction.

During the absorption process, the water is absorbed from the gaseous medium in contact with the solution, while LiBr neither consumed nor added to the solution. Thus, the phase boundary remains impermeable to LiBr, displaced by the entry of the absorbate into the solution.

While one might expect a decrease in the mass fraction w due to the absorption of water vapor at the interface, this expectation is not consistent with the observed behavior as illustrated in Fig.1(b). Initially, when the bulk solution is far from equilibrium, the absorption process occurs particularly rapidly and then slows down. This can be attributed to the fact that thermodynamic equilibrium is reached immediately at the interface during absorption. Furthermore, the diffusion of LiBr from the interior of the solution to the interface occurs at a rate comparable to that of water vapor absorption.

A. Governing equations

The binary LiBr-H_2O mixture is a Newtonian fluid where the absorbent (LiBr) is non-volatile (vanishing vapour pressure). The variable w denotes the mass fraction of LiBr. Under assumptions written above, the problem of absorption is described by the Navier–Stokes, heat, and mass transfer equations:

$$\text{div}\ \mathbf{v} = 0 \tag{2}$$

$$\frac{\partial \mathbf{v}}{\partial t} + \mathbf{v}\cdot\nabla\mathbf{v} = -\frac{1}{\rho_0}\nabla P + \nu\Delta\mathbf{v} \tag{3}$$

$$\tag{4}$$

$$\frac{\partial T}{\partial t} + \mathbf{v}\cdot\nabla T = \frac{k}{\rho_0 c_p}\nabla T \tag{5}$$

$$\frac{\partial w}{\partial t} + \mathbf{v}\cdot\nabla w = -\frac{1}{\rho_0}\nabla\mathbf{J} \tag{6}$$

here $\mathbf{J} = -\rho_0 D\nabla w$ is the mass flux, $\mathbf{v} = [V_x, V_y]$, P, T, are the velocity, the pressure and the temperature, t is the time, $\mathbf{g}$ is the gravity. The thermal β_T and solutal β_w expansions are defined as $\beta_T = -\rho_0^{-1}\partial\rho/\partial T$, $\beta_w = \rho_0^{-1}\partial\rho/\partial w$.

The aspect ratio, defined as length to height, is kept constant, $\Gamma = L/h = 7.5$, $L = 75$ mm and $H = 10$ mm. The thermophysical properties of the lithium bromide mixture, a high Prandtl liquid $Pr = 19$, are given in Table 1.

B. Boundary conditions

Interface: The interface is ideally flat and without surface waves, corresponding to the limit of large surface tension. The quantitative comparison of the interface velocity obtained in our model with the experiment[14] indicates that the flow dynamics is well captured under the flat interface assumption.

a) Vapour pressure equilibrium is assumed at the free surface, which means that the vapour pressure of water (H_2O) in the liquid phase is equal to the pressure of water vapour in the gas phase at the free surface. At the interface, the equilibrium mass fraction w_e is assumed to be the function of temperature $w_e = f(T)$, as stated by Eq. (1). Commonly, in numerical simulations the relation (1) is used in the inverse form as $T_e = f(w_e)$

$$T_e = A_1 + A_2 w_e \tag{7}$$

The value of the coefficients A_1 and A_2 are given in Table I (last line).

b) Vapour-liquid equilibrium in presence of absorption leads to the coupling of the heat and mass fluxes (H_{abs} is the heat of absorption, m_{abs} is the absorbed mass flux)

$$k\frac{\partial T}{\partial y} = m_{abs}H_{abs}, \tag{8}$$

$$(a)\ m_{abs} = -\frac{\rho D}{w}\frac{\partial w}{\partial y} \quad \text{or} \quad (b)\ m_{abs} = -\rho D\frac{\partial w}{\partial y}$$

Equation (8) shows that the mass flux m_{abs} can be defined in two different ways. The condition (8a), so-called 1D diffusion, considers that the penetration of the absorbate changes the volume of the solution, so the flat upper boundary begins to move[3,26]. When using condition (8b), the interface motion is disregarded. Correspondingly, the layer thickness remains

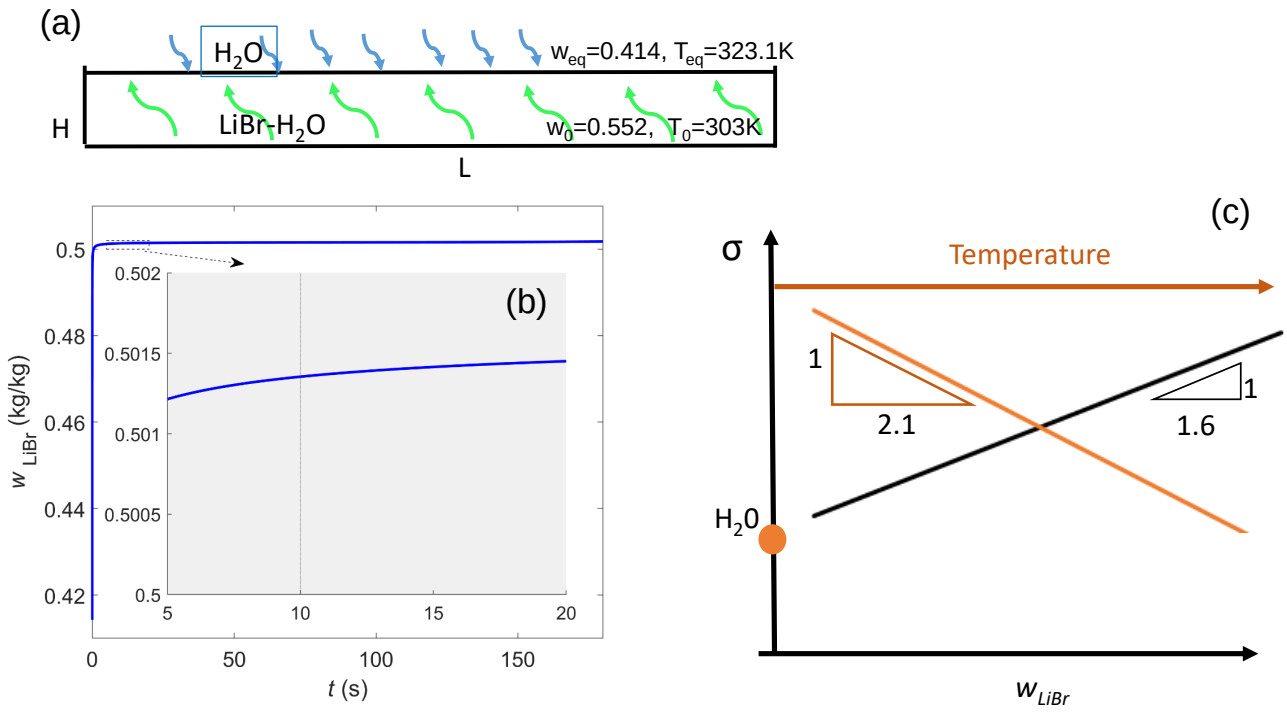

FIG. 1. Particularity of LiBr-Water mixture absorbing water vapor. (a) Sketch of diffusion/absorption process; (b) Evolution of mass fraction at the interface during absorption. Initially the curve goes almost along the vertical axis. The inset shows the slowdown in the change in w a few seconds after the process begins. (c) Dependence of the LiBr surface tension (σ) on composition and temperature.

constant and the velocity field in the pool is not affected by the interface displacement.

In this study we use boundary condition (8a) assuming that the characteristic time of the interface motion is much larger than the hydrodynamic timescale. The interface deformation is not considered, then $V_n = 0$. This assumption was also used in previous simulations by different authors[9,10].

d) Balance between viscous and capillary forces is imposed in the presence of Marangoni convection

$$\mu \frac{\partial V_x}{\partial y} = \sigma_T \frac{\partial T}{\partial x} + \sigma_w \frac{\partial w}{\partial x} \tag{9}$$

e) The remaining boundary conditions are as follows (here the subscripts n refer to the normal component):
- No-slip condition for velocity along the lateral and bottom walls $\mathbf{v} = 0$.
- Adiabatic conditions on the lateral and bottom walls $\partial T/\partial n = 0$.
- The lateral and bottom walls are impermeable $\partial w/\partial n = 0$.

C. Initial conditions:

The pool of LiBr-water at $t = 0$ is kept at $T_0 = 303\,\mathrm{K}$ and its mass fraction is $w_0 = 0.5522\,\mathrm{kg/kg}$. These initial conditions are far from the equilibrium conditions determined by the equilibrium linear function, Eq. (7). The equilibrium condition at $P = 2.3\,\mathrm{kPa}$ corresponds to $w_e = 0.4143\,\mathrm{kg/kg}$ and $T_e = 323.11\,\mathrm{K}$, respectively. The liquid at the interface reaches thermodynamic equilibrium with the vapour immediately upon contact at $t = 0$, but it takes time for the effect to diffuse into the bulk liquid. Since we consider one-phase problem, at the initial time we impose at the interface $T(t = 0) = T_e$, and $w(t = 0) = w_e$.

Flow perturbation:

Here we examine absorption process affected by local perturbation of the mass fraction at the interface, leading to the appearance of Marangoni flows. It is important to note that this composition perturbation is imposed 10 seconds after the absorption process commences, with an instantaneous and singular effect. Within the localized perturbed region, the mass fraction distribution is modeled as a cosine function:

$$w = w_{0,in} - \frac{\Delta w}{4}\left[1 - \cos\left(\frac{1000\pi}{3}x + \frac{\pi}{2}\right)\right]^2 \tag{10}$$

$$34.5\ \mathrm{mm} \le x \le 40.5\ \mathrm{mm}.$$

Correspondingly, $w_{0,in}$ is the mass fraction on the interface at $t = 10\,\mathrm{s}$. A local perturbation of concentration in middle with a radius of $R_0 = 3\,\mathrm{mm}$ with max value $\Delta w = 0.002\,\mathrm{kg/kg}$ leads to a subsequent decrease in the equilibrium temperature.

We chose the squared cosine function for analyzing localized perturbations for following reasons. The difference between cosine and its square lies in the width of the peak, which is narrow in the case of squared cosine. We assume that the

perturbation of absorption is strong locally. In addition, its smooth edge profile of the squared cosine helps mitigate potential numerical instability.

D. Numerical approach

Governing equations (2)-(6) with boundary conditions (6)-(9) are solved in dimensional variables using the commercial software ANSYS Fluent 23.1 based on the Finite Volume Method. For this purpose, the SIMPLE scheme for pressure velocity coupling is used. Second order for pressure discretization and second order upwind for energy, momentum and species transport discretization are employed. Moreover, gradients are evaluated using Green-Gauss Node Based scheme.

The code validation and mesh independence analysis, discussed in our previous paper with gravity[1] , remain consistent with the current investigation. During the first ten seconds, when uniform absorption occurs, no convection is present, the numerical solution was validated by comparison with the analytical solution proposed by Nakoryakov et al.[3]. The uniform absorption is unaffected by gravity.

When convection begins, the primary challenge is the slow diffusion combined with the fast Marangoni flow, as the Lewis number is around 90. The mesh near the surface must be sufficiently fine to accurately resolve this issue. For the convection phase, the numerical code was validated by comparison with experimental results[14]. Due to the opposite signs of Ma_s and Ma_T in the initial stage, the flow direction is toward the center, which exactly matches the flow direction observed in the experiments. Additionally, the experiments reported that the horizontal velocity reaches 0.8 mm/s at the beginning of the process[14], which is in excellent agreement with the numerical predictions. In these initial stages, the Marangoni force is the primary influencing factor, and the presence or absence of gravity does not yet play a role. Therefore, the previous code validation remains applicable to the current study.

III. RESULTS

At the initial time $t = 0$, the mass fraction of LiBr at the interface is lower than in the bulk solution and the temperature is higher, see the sketch of absorption in Fig. 1. The composition perturbation is imposed 10 s after the start of the absorption process, with an immediate and singular effect. A minor disturbance of the mass fraction at the center of the absorbing interface, as given in Eq. (10), results in the formation of a localized area with a lower LiBr mass fraction and a change in surface tension (σ). At the remainder of the interface σ remains unchanged. The convective instability is triggered by this local perturbation of the uniform absorption.

The surface tension of the LiBr mixture varies with both w and T, with these dependencies exhibiting opposite directions, as illustrated in Fig.1(c): increasing with mass fraction and decreasing with temperature. The slope of the temperature gradient is higher than that of the mass fraction, thereby controlling the Marangoni flows. The opposite signs of the surface tension gradients with respect to w and T complicate the understanding of the flow dynamics. The individual contributions of the solutal and thermal Marangoni stresses, which significantly diminish the net effect because they act in opposite directions can be seen later in Fig. 4(b).

TABLE I. Physical properties of the LiBr-water mixture with content of LiBr in mass fractions w_0=0.5522 ($\mathrm{kg\,kg^{-1}}$) at T_0 = 303 K. All data are taken from ref.[9]. The Prandtl number $Pr = \nu/\alpha = 19$.

Diffusion	D [m^2/s]	$1.430 \cdot 10^{-9}$
Thermal diffusivity	α [m^2/s]	$1.235 \cdot 10^{-7}$
Thermal conductivity	k [W/m K]	$4.38 \cdot 10^{-1}$
Latent heat	H [J/kg]	$2.568 \cdot 10^{6}$
Thermal expansion	β_T [1/K]	$3.645 \cdot 10^{-4}$
Solutal expansion	β_w [1/wt%]	$-1.109 \cdot 10^{-2}$
Dynamic viscosity	μ [kg/m s]	$3.830 \cdot 10^{-3}$
Kinematic viscosity	ν [m^2/s]	$2.358 \cdot 10^{-6}$
Density	ρ [kg/m^3]	$1.624 \cdot 10^{3}$
Gravity	g [m/s^2]	9.8
Surface tension	σ [N/m]	$6.00 \cdot 10^{-2}$
$\sigma_w = (\partial\sigma/\partial w)$	[N/m wt]	$1.61 \cdot 10^{-2}$
$\sigma_T = (\partial\sigma/\partial T)$	[N/m K]	$-2.1 \cdot 10^{-4}$
Equilibrium condition:	$T_e = A_1 + A_2\, w_e = 242.6 + 145.8 \cdot w_e$	

Although the problem is solved in dimensional variables, it is useful to introduce the thermal (Ma_T) and solutal (Ma_s) Marangoni numbers, which quantify the strength of the flow

$$Ma_s = \frac{|\sigma_w| h^* \Delta w}{\mu\, D}, \quad Ma_T = \frac{|\sigma_T| h^* \Delta T}{\mu\, \alpha}, \tag{11}$$

here h^* is the characteristic length scale associated with the interface where the gradients occur. The absorption problem also depends on the Lewis number (Le), which defines the ratio of thermal to mass diffusivity, and the Prandtl number, which relates viscosity to thermal conductivity (Pr). These numbers remain constant throughout the study:

$$Le = \frac{\alpha}{D} \sim 90, \quad Pr = \frac{\nu}{\alpha} = 19. \tag{12}$$

IV. STABLE RIM FORMATION.

As the evolution of the flow is controlled by the temperature gradient, the generated motion is initially directed towards the center, which is consistent with experimental observations[11]

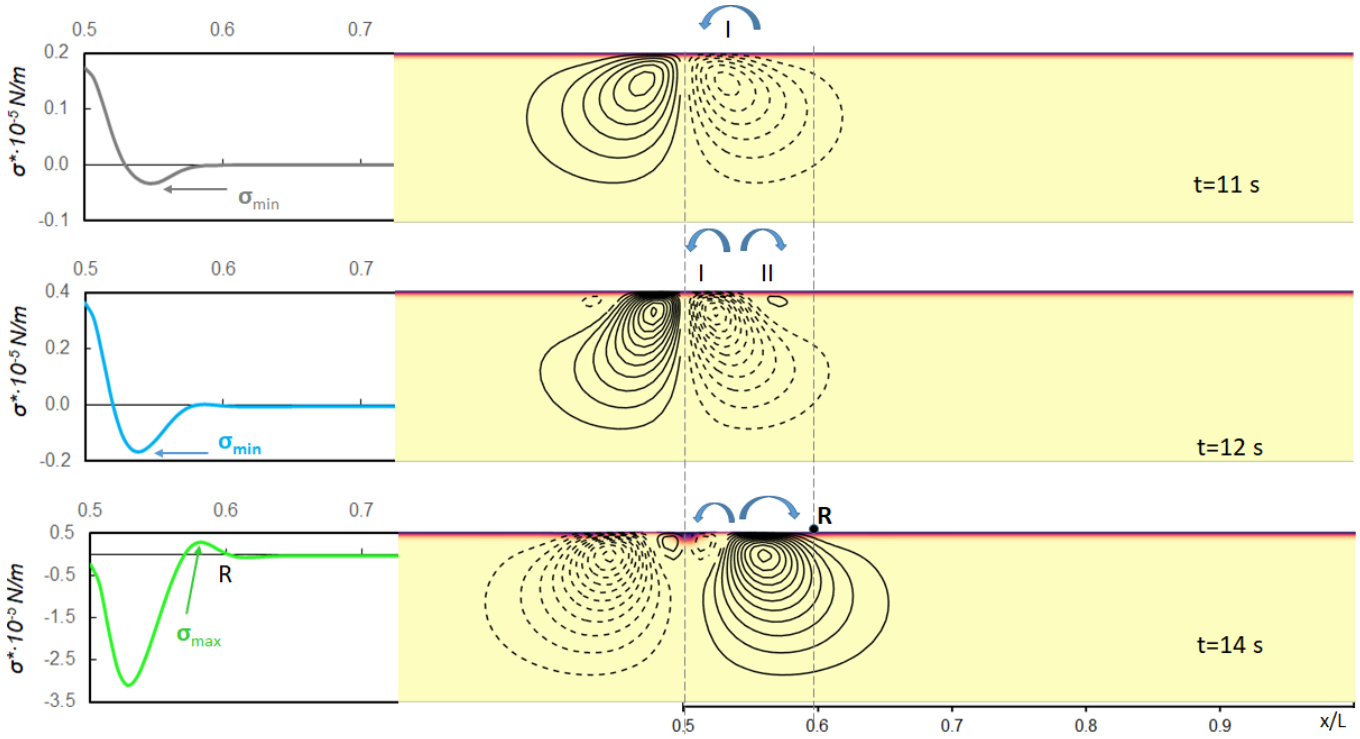

FIG. 2. The occurrence of a flow pattern in an absorbing binary mixture which bears resemblance with that one observed in the 'coffee-ring' phenomenon. The snapshots illustrate the evolution of Marangoni flow and the formation of the rim with radius R. The large blue arrows indicate the flow direction. Clockwise (counterclockwise) circulation in the vortices is indicated by solid (dashed) curves. Vertical dashed lines over all snapshots depict the center of the cell ($x/L = 0.5$) and the radius of stable rim ($x/L \sim 0.58$). The left side of the snapshots displays the distribution of relative surface tension ($\sigma^* = \sigma - \sigma_0$) along the central part of interface ($0.5 \leq x/L < 0.7$) at the same time moments as the flow pattern. The elevated surface tension shown by arrow at $t = 14$ explains the pinning effect during Marangoni spreading. In the snapshots w is represented by colors, with red indicating a lower mass fraction.

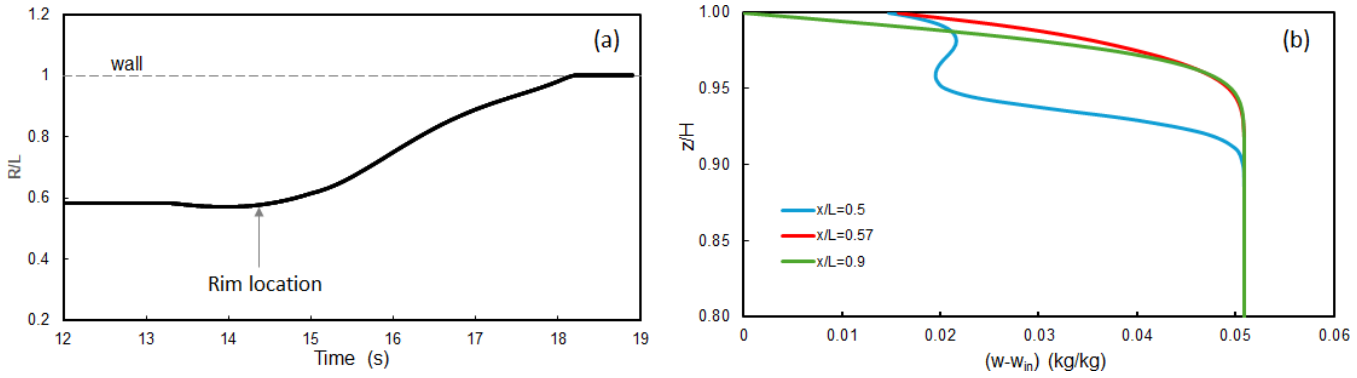

FIG. 3. (a) The occurrence of the rim and Marangoni spreading phenomenon characterised by the displacement of the point with zero velocity (V_x). (b) The distribution of w in height at three horizontal positions: $x/L = 0.5, 0.57$ and 0.9 at $t = 16.6$ s. The two latter positions are indicated by arrows and designated with letters p1 and p2 in Fig 5. The blue curve shows that at the cell centre, the LiBr-poor mixture extends deeper. The graph clearly shows that the mass fraction in the bulk is significantly higher than at the absorbing interface.

in the ground laboratory. In the initial stages, the primary influencing factor is the Marangoni force, and the presence or absence of gravity does not yet play a role. The snapshot at $t = 11$ s in Fig. 2 illustrates that the capillary flow draws down the LiBr-poor mixture, while the return flow carries a cooler mixture rich in LiBr to the interface. Over time, this creates a region with a reduced surface tension, with the minimum located outside of perturbed area, at $x/L = 0.547$, as indicated by the gray curve at the left part of snapshot at $t = 11$ s. The distribution of a relative surface tension shown on the left side

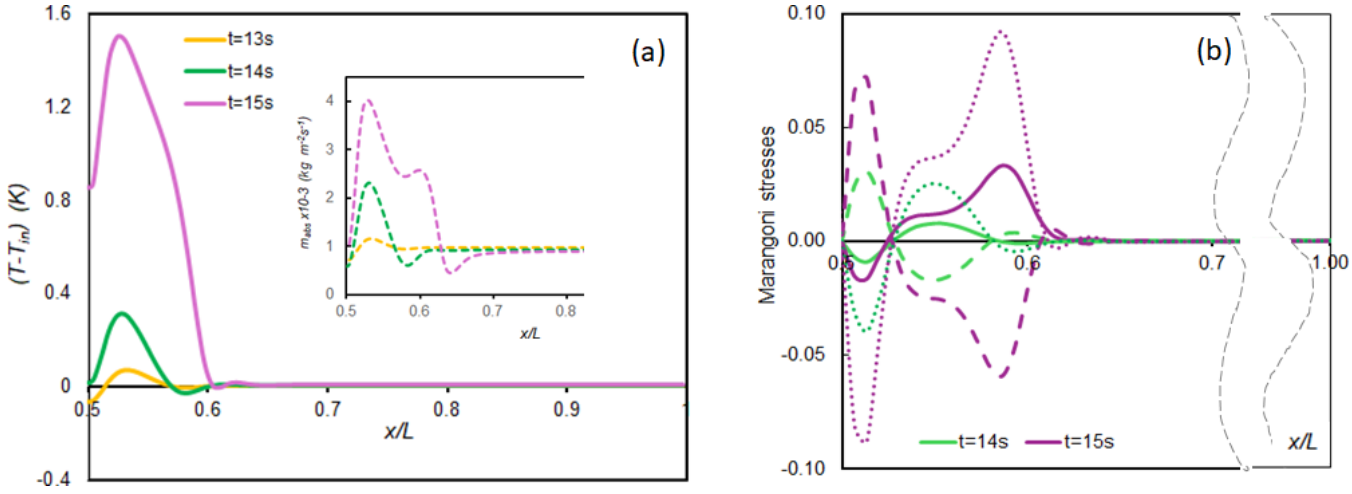

FIG. 4. (a) Temperature $(T - T_{in})$ distribution along the interface and (insert) the absorbed mass flux at selected times, highlighting the pinning of the rim and the onset of Marangoni spreading (b) The Marangoni stresses created by the variation in w and T: $\tau_w = (\partial\sigma/\partial w)(\partial w/\partial x)$ (the dashed curves), $\tau_T = (\partial\sigma/\partial T)(\partial T/\partial x)$ (the dotted curves) and the net stress $\tau = \tau_w + \tau_T$ (the solid curves). All graphs indicate that between 14 and 15 s, the Marangoni flow evolves sharply. The grey dashed curves in panel (b) indicate the interruptions in cell length to focus on the central region, where changes in Marangoni stresses occur.

in Fig. 2 is calculated as follows:

$$\sigma^* = \sigma - \sigma_0 = \sigma_T(T - T_{in}) + \sigma_w(w - w_{in}), \qquad (13)$$

the values of T_{in} and w_{in} are taken at the interface at $t = 10$ s. Over time, $|\sigma^*_{min}|$ deepens and shifts towards the centre. For example, the minimum value of σ^*_{min} at $t = 12$ s is located at $x/L = 0.547$, whereas at $t = 14$ s it is located at $x/L = 0.527$. This shift is accompanied by increasing gradients in the surface tension on either side of the extreme value, which have different signs, as can be seen from the σ^* profile at $t = 12$ s and later. In response, a second Marangoni vortex emerges with opposite direction of circulation, as evidenced by region II in the snapshots at $t = 12$ s. On a short time scale, the growing gradients in σ strengthen the Marangoni flow in both directions. Over time, the vortex with a positive direction of circulation grows, while the original one with a negative direction of circulation decays, see a snapshot at $t = 14$ s. Two opposite vortices destroy the homogeneity of the boundary layer in terms of mass fraction. As a result, a small plume-like structure with a lower mass fraction (red colour) is forming at the center, aligned with the shape of the diminishing vortex.

Of particular interest is the formation of a motionless rim along the periphery of the growing vortex. The flow pattern with the presence of the rim resembles the spreading of a drop on a deep liquid layer and the well-known 'coffee-ring' phenomenon commonly observed in evaporating binary liquid droplets[15–17,27]. In their seminal paper on the 'coffee ring' effect[15], Deegan and co-authors demonstrated that a ring forms because the contact line of a droplet is pinned, requiring liquid to be drawn from the center to the edge to maintain the contact line as evaporation proceeds. Here, we observe a similarity between that evaporation-driven process and the phenomena occurring during LiBr-water absorption. This is the first occasion on which this prominent rim formation has been observed in an absorbing binary mixture.

The rim formation and following Marangoni spreading are illustrated in Fig. 3(a) as a function of R(t), where R is the point with zero velocity V_x on the interface. The figure shows that for several seconds, the flow was constrained in the area with $x/L = R_0 \approx 0.583$, due to the pinning of the rim by the oncoming weak convection. After the initial formation, the rim slightly retracted between 13.3 s and 14.5 s, a behavior also seen in drop spreading on a deep liquid layer[28]. Figure 3(b) highlights that the variation in mass fraction during the stable rim existence and its spreading at later times occurs within a very thin subsurface layer.

Unlike the numerous studies of evaporating droplets, the formation of the rim in our observations is not directly linked to the propagation of an initial perturbation. This formation is associated with the emergence of a capillary wave (with elevated temperature and mass fraction) arising as a secondary effect of the initial perturbation (see the yellow and green curves in Fig. 4(a)). The rim formed at a distance from the disturbed region is characterised by an almost zero velocity. The net Marangoni stress, shown by the solid green curve in Fig. 4b, exhibits a small negative value at $0.58 < x < 0.60$, which is responsible for the pinning effect. The combined effects of absorption, heat release and the equilibrium condition influence the surface tension and make this phenomenon possible.

At the interface, temperature and mass fraction are related by the equilibrium condition. Beneath the interface, heat transfer occurs at a much faster rate than mass transfer. This leads to a situation where, at the edge of the growing dominant vortex, starting from $t = 12$ s, the surface tension exhibits an inflection: the small peak and then tiny minimum. The peak is highlighted by the green arrow on the graph of σ^* at $t = 14$ s. The occurrence of the inflection in the surface tension results in a weak flow in the direction opposite to the main vortex. It serves to impede the flow and stabilize the rim. The tem-

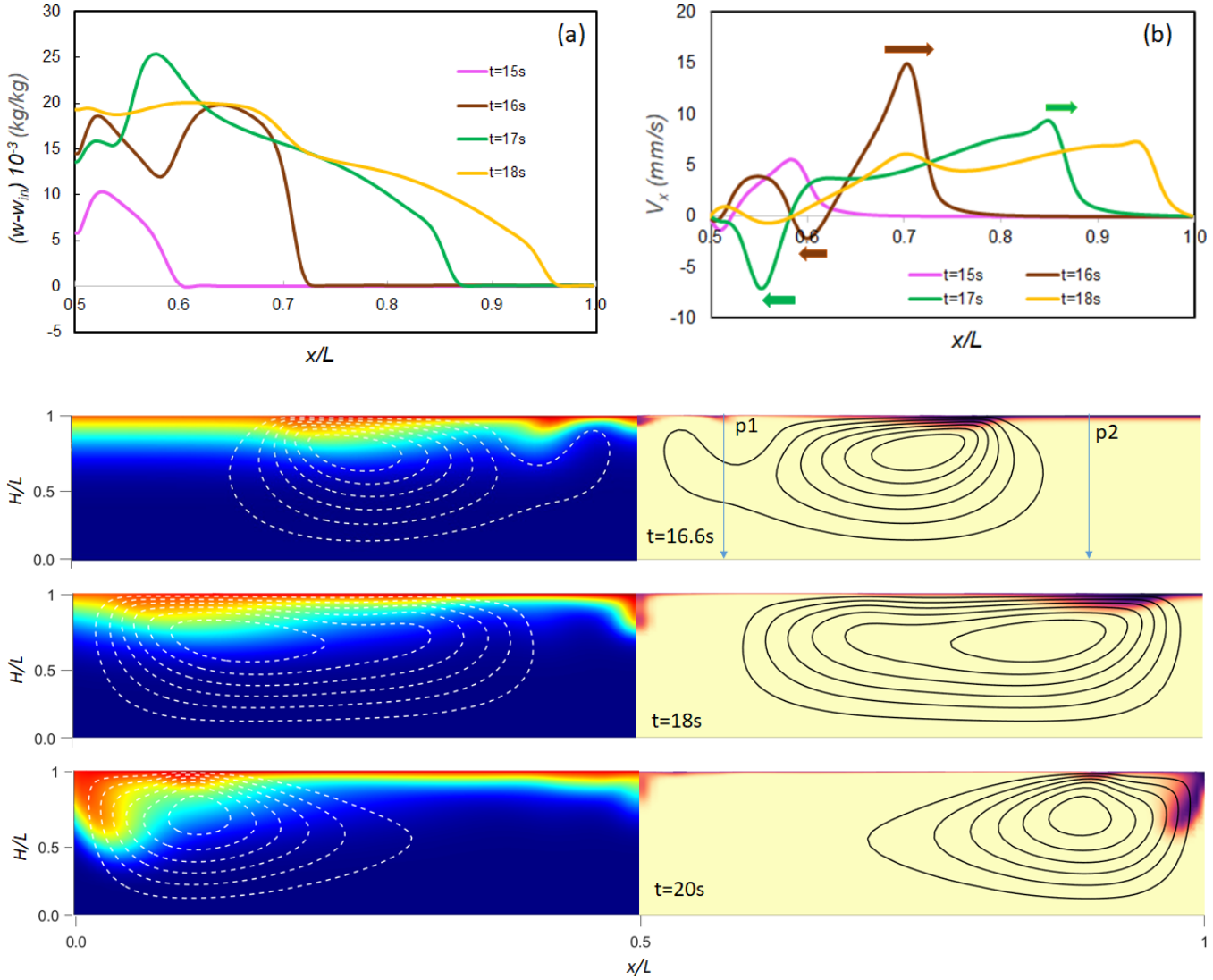

FIG. 5. Temporal evolution of (a) mass fraction $(w - w_{in})$ and (b) velocity V_x along the interface. Recall that $w_{in} = 0.5014$ kg/kg represents the mass fraction on the interface at $t = 10$ s. For better clarity, the mass fraction and velocity are shown in the half-cell, given that the flow is symmetric. The snapshots present two sets of data, displaying the temperature and mass fraction on the left and right sides, respectively. They illustrate the development of the Marangoni convection at representative time moments. This presentation demonstrates the similarity of T and w in the vicinity of the interface, where they are related by equilibrium condition. The snapshot at $t = 20$ s illustrates the formation of an area with low w near the side wall, which will later serve the role of perturbation similar to the initial one. The dashed level lines indicate the counterclockwise circulation of the vortices. The lines p1 and p2 indicate the coordinates at which the vertical distribution of w is shown in Fig. 3(b)

perature profile and absorbed mass flux at $t = 14$ s shown in Fig. 4(a) (the green curves) further illustrate the pinning effect.

V. SPREADING DYNAMICS.

Until $t = 15$ s, the absorption behaviour around the peak value is smooth, without skips. A marked increase in the absorption between 14 s and 15 s leads to a sharp rise in Marangoni stress, as illustrated in Fig. 4. At this time, the absorption profile as well as Marangoni stresses, exhibits an inhomogeneous pattern, indicating spatially variable surface tension. This acts as a precursor to the new phenomenon. The Marangoni numbers, which have opposite signs, at $t = 14s$ were $|Ma_s| = 140$ and $|Ma_T| = 230$, but increased by almost 5 times at $t = 15s$. The shear stress at $t = 15$ s is enough powerful to create a flow that overcomes the pinning and Marangoni spreading starts. The velocity of the advancing rim demonstrates a gradual increase and subsequent decrease over time, as evidenced by the successive peaks of V_x in Fig 5(b) and at $t = 18$ s it reaches the wall.

From the perspective of the LiBr/water binary mixture, this spreading can be considered as the propagation of a wave over

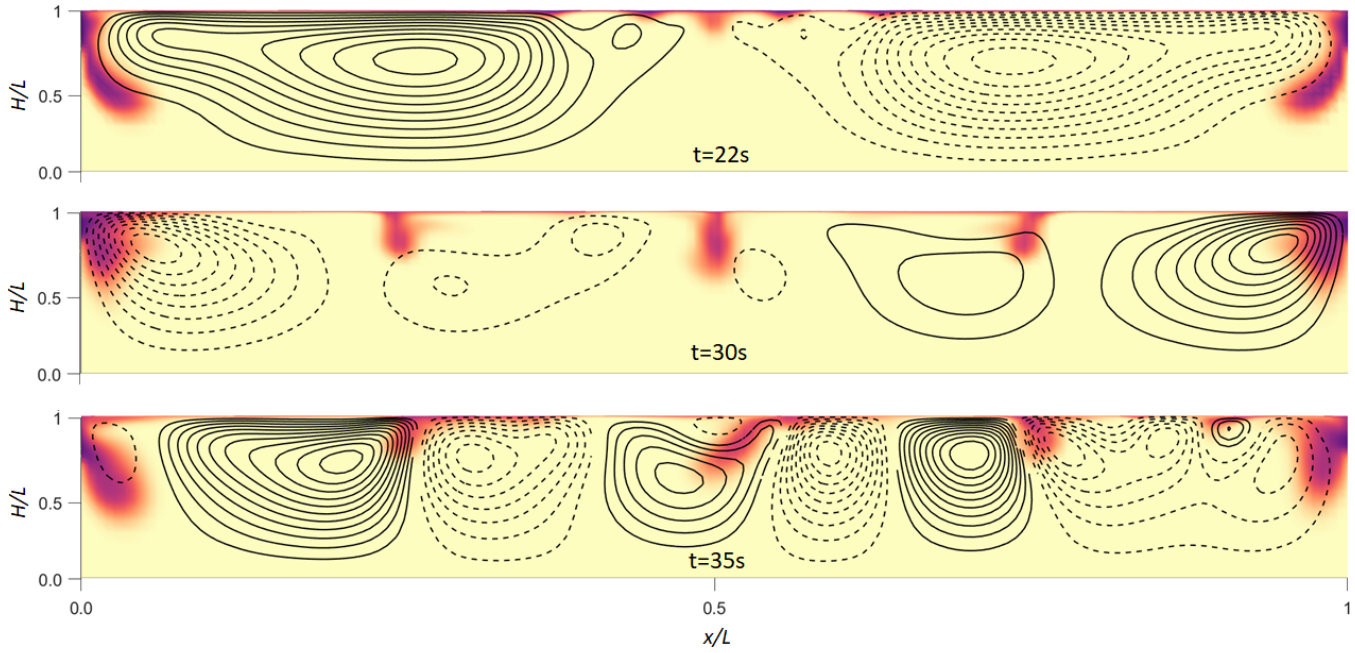

FIG. 6. The flow field and mass fraction at representative time moments. The pattern at $t = 22$ s represents the results of flow development when the side wall region with low w plays a role analogous to the initial disturbance. The pattern at $t = 30$ s shows the main plumes. The pattern at $t = 35$ s demonstrates the symmetry breaking.

the interface with an increased temperature as well as mass fraction shown by snapshots in Fig 5. In the bulk flow, the dominant vortex rapidly enlarges. At the subsurface, the initial wave is followed by the formation of a region with lowered w (a prototype of a finger/plume), as depicted by "p1" ($x/L = 0.58$) in the snapshot at $t = 16.6$ s. While the primary wave continues to spread towards the wall, the newly-formed eddy associated with the plume retracts, thinning the concentration boundary layer behind it. If the mixture at the interface differed from the mixture in the pool, a rupture of the film could occur. Thus, this type of instability exhibits similarities to the previously observed Marangoni bursting of an evaporating droplet[28–31].

The mass fraction and velocity profiles at successive times ($15\,\text{s} \leq t \leq 18\,\text{s}$) in Fig 5 (a)-(b) further clarify the development of instability. The retracting eddy is accompanied by the formation of a plume with a reduced mass fraction, which appears as a minimum on the brown curve in Fig. 5(a) at $x/L = 0.58$. The velocity of the retracting plume is less than that of the primary wave, as evidenced by the peaks with negative and positive velocity, highlighted by arrows near the brown curve in panel (b).

The motion towards the center speeds up, as shown by the comparison of the peaks in negative velocity at $t = 16$ s and $t = 17$ s. This acceleration brings a more concentrated mixture from the subsurface, leading to the formation of a w peak later, see green curve in panel (a). At the moment when the primary wave reaches the wall, this plume collapses with what was in the center and forms a large columnar-shaped plume, see snapshot at $t = 18$ s. The velocity in the central region almost fades and remains at this reduced level for a while, as seen in snapshot at $t = 20$ s. The wall vortex continues to transport the lower w towards the wall in the subsurface, resulting in the formation of a region with a LiBr-poor mixture that thickens and detaches from the wall with depth. Over time, the position of this region remains static.

Recall that the reddish colour in the all snapshots of mass fraction corresponds to w low value. In order to maintain consistency throughout our discussion, let us return to Fig. 3(b), which shows the distribution of w in height at three horizontal positions at $t = 16.6$ s (identical in time to Fig. 5 top snapshot). This figure, using an enlarged scale, demonstrates that w exhibits significant variation in a thin surface layer affected by absorption. However, due to resolution limitations, this change is not visible in the snapshots. The green curve, representing $(w - w_{in})$ profile in the undisturbed part of the cell at position $p2 : (x/L = 0.9)$, exhibits a nearly zero value at the interface. The small variation of the w is associated with a continuous and uniform absorption. In contrast, the blue and red curves, which traverse the plumes, are nearly identical at the interface and exhibit a significantly higher value than the green curve, with a difference of $\Delta w = 17 \cdot 10^{-3}$kg/kg. This difference is seen in Fig. 5(a) when we discuss the elevated mass fraction. Furthermore, the blue curve shows that, at the center of the cell, the region with a LiBr-poor mixture extends to a considerable depth, thus illustrating the amplitude of the plume.

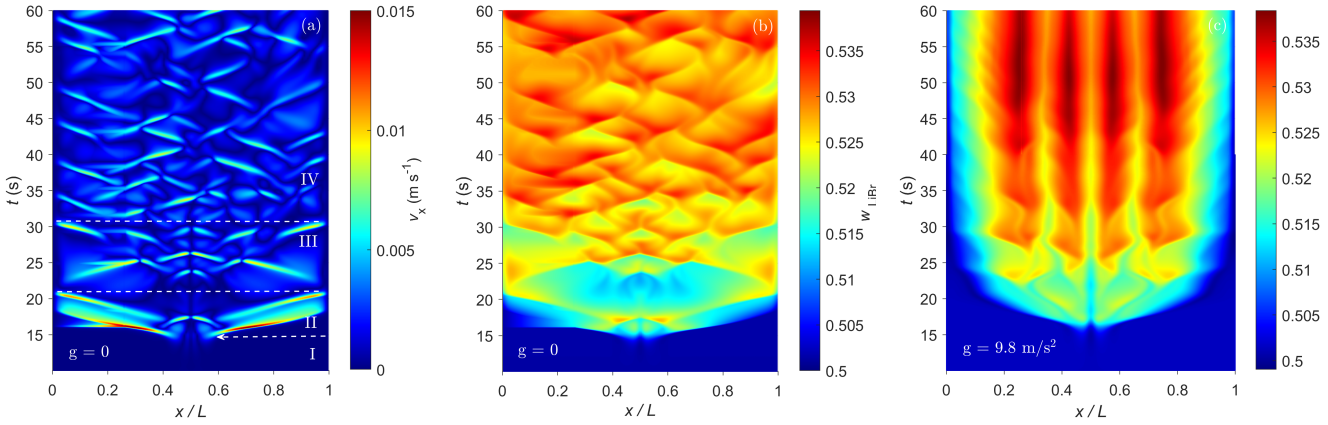

FIG. 7. The space-time maps for (a) the interface velocity (absolute value) and (b) mass fraction w at g=0. (c) The map of w when $g = 9.8\text{m/s}^2$. The maps at $g = 0$ exhibit a strongly non-stationary picture while weakly oscillating stationary patterns can be seen at $g = 9.8\,\text{m/s}^2$.

VI. OSCILLATORY INSTABILITY AND SYMMETRY BREAKING

After an area with a distinct low value of mass fraction forms near the side wall ($t = 20\,$s in Fig. 5), it plays a role similar to the initial perturbation at the center, though in the opposite direction. The evolution of the flow pattern mirrors the one depicted in the snapshot at $t = 12s$ in Fig. 2 but in the reverse direction. On the periphery of an existing vortex with a positive direction of circulation, a region with elevated surface tension forms around $x/L \sim 0.8$, giving rise to a vortex with opposite circulation. The newly formed vortex rapidly expands and eventually occupies the entire space, as illustrated by the snapshot at $t = 22\,$s in Fig. 6.

From this time on, the fragmentation of larger vortices into smaller ones begins, followed by their subsequent merging, which leads to the formation of three to seven finger-like plumes as illustrated by snapshots in Fig. 6. The dynamics of Marangoni flow is controlled by the continuous change in the surface tension of the LiBr/water mixture due to the non-uniform absorption. This phenomenon is characterized by non-periodic oscillatory instability. The central plume, which is mostly static, is columnar in shape, exhibiting a somewhat narrow isthmus and an elongated form as it descends into the LiBr mixture. Two of the plumes are situated close to the side walls, while the remaining ones are in continuous motion, undergoing a process of merging and splitting, as illustrated in Fig. 6. These intermediate mobile plumes undergo a continuous change in shape, evolving from a symmetric to an inclined columnar configuration with a one-sided tail, as seen in the snapshot at 30 s. At some moments (not shown), they take on the shape of an elongated lens, occupying almost the entire subsurface. The repetitive increase and decrease in the surface mass fraction/temperature leads to the displacement of plumes through an imbalance in surface tensions. Starting from 29 s, the symmetry of the flow is broken, and the different plumes take on various shapes in terms of height, width, and inclination, as illustrated in the snapshot at 35 s.

The conditions under which the behavior described above is observed can be summarised as follows: non-homogeneous absorption in a binary mixture, considerable Marangoni stresses, and a freely moving regions with an essential change in w. It is possible that the term "plume" is not an accurate description of these regions of lower w. For example, in the presence of gravity[1], such plumes (regions with lower w) exhibited a clear mushroom-shape.

VII. OVERVIEW AND COMPARISON WITH GRAVITY CASE.

The non-linear behaviour of the system is outlined by the phase plane trajectories at different time intervals in Fig..

Figure 7 summarises, using space-time maps, the various time regimes in which an interface responds to the action of absorption and Marangoni convection. The observed regimes, most of which are described above, are separated by white dashes on the space-time velocity map in panel (a). While we only show the regime separation on the velocity map, the discussion extends the same regimes to the mass fraction map in panel (b). In the first regime, the arrow from the right side indicates the radius of a stable rim at the end of its existence. In the second regime, the light blue colour on the velocity map indicates fast Marangoni spreading. A careful examination of the mass fraction map in this regime shows that w has deep local minima in some regions, suggesting a potential analogy with film rupture when a drop spreads on an oil bath [29]. As we consider the spreading of the wave with increased w over the same mixture, only a thinning and disruption of the boundary layer in w can be observed. Regime III is characterized by the development of non-periodic oscillations, ending with the breaking of symmetry. The evolution of non-stationary patterns is characteristic of Stage IV, which is easier to follow in the mass fraction map. In this regime, localized objects (quadrangles or small regions where "plumes" move and change shape, outlined by thin red lines) form within the region and move to the left and right, colliding with each other and disappearing at the boundaries. The states on both sides

of the red line are of the same nature, creating "breathing" and oscillating cells. These quadrangles are fairly regular, with a tendency for the number of thin red lines to decrease over time and for cell coarsening to occur.

In contrast to the case of $g = 0$ with non-stationary patterns, the time-space map at $g = 9.8\,\mathrm{m/s^2}$ in panel (c) shows stationary, weakly oscillating patterns. The presence of buoyancy-driven forces produces a strong counterbalance to the Marangoni flow, generally reducing the interface velocity[1]. Consequently, gravity influences the ordering of patterns, establishing both temporal and spatial periodicity in the system. The central part of the time-space map at $g = 9.8\,\mathrm{m/s^2}$ is occupied by vertical bands associated with plumes, which exhibit minimal changes over time, while a periodic structure is established near the wall with an almost constant period. Such a strong effect of gravity on the absorption dynamics can be explained by the relatively weak Marangoni stresses, since the thermal and solutal Marangoni stresses have opposite signs and reduce the net effect.

All the patterns, with or without gravity, exhibit the absorption-limited nature of the instability, illustrating the gradual loss of energy over time.

VIII. CONCLUSION

We have investigated the convective instability in a LiBr-water binary mixture using numerical simulations, initiated by a local perturbation of uniform absorption at the cell center. The decrease in mass fraction triggered solutal convection, which subsequently led to a local temperature change and induced thermal Marangoni convection. To isolate and gain a deeper understanding of the interaction between the Marangoni effect and absorption, we examined the behavior of the LiBr-water binary system in a microgravity environment.

For the first time, we observed the formation of a stable rim in an absorbing binary mixture, where the flow pattern resembles the dynamics of an evaporating droplet on a substrate or a deep liquid layer. Additionally, we noted a slight contraction of this rim, followed by rapid Marangoni spreading. This suggest a similarity between the Marangoni effect during evaporation and LiBr absorption.

However, in the finite-length geometry of our cell, this similarity with evaporating binary mixtures in extended systems ceases when the advancing rim reaches the side walls. We then observe a breakdown of symmetry around the center of the cell, followed by non-periodic oscillations. At late times, the cell is occupied by growing in size non-stationary, although regular, patterns.

The presence of buoyancy-driven forces introduces a competing effect against the Marangoni flow, altering the absorption dynamics. We hope that our study will contribute to a better understanding of the observations made in experiments with surfactants, where the Marangoni effect strongly dominates over buoyancy.

Acknowledgments The work is supported by Elkartek program (KK-2023/00041- MMASINT) and Research Group Program (IT1505-22) of the Basque Government, and Grant PID2021-124232OB-I00 (Treated) funded by MCIN/AEI/10.13039/501100011033 of the Spanish Government and by "ERDF A way of making Europe".

The authors have no conflicts to disclose

P.F.A.: Data Curation, Formal Analysis, Software and Writing/Original Draft Preparation; M.M.A.: Data Curation, Investigation and Visualization; A.N: Methodology, Validation and Writing/Reviewing and Editing; MM.B: Funding Acquisition, Validation and Writing-Review and Editing; VS: Funding Acquisition, Conceptualization, Supervision and Writing/Review and Editing. The data that support the findings of this study are available from the corresponding author upon reasonable request.

[1]P. F. Arroiabe, M. Martinez-Agirre, A. Nepomnyashchy, M. M. Bou-Ali, and V. Shevtsova, "The effect of small perturbation on dynamics of absorptive LiBr-water solution," Phys. Fluids **36**, 022119 (2024).

[2]W. Wu, B. Wang, W. Shi, and X. Li, "Absorption heating technologies: A review and perspective," Applied Energy **130**, 51–71 (2014).

[3]V. Nakoryakov and N. Grigoreva, "Nonisothermal absorption in thermotransformers," J. Engineering Thermophysics **19(4)**, 196–271 (2010).

[4]P. Arroiabe, M. Martinez-Agirre, and M. M. Bou-ali, "Numerical analysis of different mass transfer models for falling film absorbers," Int. J. Heat Mass Transfer **182**, 121892 (2022).

[5]C. Beal, E. Gardner, and N. Menzies, "Process, performance, and pollution potential: A review of septic tank-soil absorption systems," Aust. J. Soil Res. **43** (2005).

[6]J. Xie, D. Wang, L. Liu, T. Shao, H. Zhou, and D. Zhang, "An overview of flue gas SO2 capture technology based on absorbent evaluation and process intensification," Ind. Eng. Chem. Res. **63**, 6066–6086 (2024).

[7]M. Hozawa, M. Inoue, J. Sato, T. Tsukada, and N. Imaishi, "Marangoni convection during steam absorption into aqueous libr solution with surfactant," J. Chem. Eng. Jpn. **24**, 209–214 (1991).

[8]D.-H. Rie and T. Kashiwagi, "Experimental study of steam absorption enhancement in accordance with interfacial turbulence into aqueous solution of LiBr: The influence of a noncondensable gas," JSME Int. J. Ser. 2, Fluids engineering, heat transfer, power, combustion, thermophysical properties **34**, 502–508 (1991).

[9]H. Daiguji, E. Hihara, and T. Saito, "Mechanism of absorption enhancement by surfactant," Int. J. Heat and Mass Transfer **40**, 1743–1752 (1997).

[10]J. Castro, L. Leal, C. D. PÃ©rez-Segarra, and P. Pozo, "Numerical study of the enhancement produced in absorption processes using surfactants," Int. J. Heat Mass Transf. **47**, 3463–3476 (2004).

[11]N. Bufetov, R. Dekhtyar, and V. Ovchinnikov, "An experimental investigation of thermocapillary convection in solution of lithium bromide with non-isothermal absorption," Vestnik of MSTU, in russian **19**, 673â€“679 (2016).

[12]J. S. Kim, H. Lee, and S. I. Yu, "Absorption of water vapour into lithium bromide-based solutions with additives using a simple stagnant pool absorber," Int. J. Refrig. **22**, 188–193 (1999).

[13]V. E. Nakoryakov, N. I. Grigoryeva, N. S. Bufetov, and R. A. Dekhtyar, "Heat and mass transfer intensification at steam absorption by surfactant additives," Int. J. Heat Mass Transf. **51**, 5175–5181 (2008).

[14]N. S. Bufetov and R. A. Dekhtyar, "Investigation of transient regimes with steam absorption by water solution of lithium bromide," Thermophysics and Aeromechanics **28**, 125–136 (2021).

[15]R. D. Deegan, O. Bakajin, T. F. Dupont, G. Huber, S. R. Nagel, and T. A. Witten, "Capillary flow as the cause of ring stains from dried liquid drops," Nature **389**, 827–829 (2000).

[16]R. G. Larson, "Re-shaping the coffee ring," Angew. Chem., Int. Ed. **51**, 2546–2548 (2012).

[17]X. Chen, N. Zhu, Y. Wakata, W. Wang, Z. Song, and X. Chao, "Full-field vapor concentration and temperature field measurement of an evaporating ethanol-water binary sessile drop by tomographic laser absorption spectroscopy," Phys. Fluids **35**, 123313 (2023).

[18] A. D. Dussaud and S. M. Troian, "Dynamics of spontaneous spreading with evaporation on a deep fluid layer," Physics of Fluids **10**, 23–38 (1998).
[19] F. Jia, T. Wang, X. Peng, and K. Sun, "Three stages of Marangoni-driven film spreading for miscible fluids," Phys. Fluids **34**, 121705 (2022).
[20] A. Pant, B. A. Puthenveettil, and S. K. Kalpathy, "Marangoni plumes in miscible spreading," Phys. Fluids **35**, 032107 (2023).
[21] J. Zhang, R. P. Behringer, and A. Oron, "Marangoni convection in binary mixtures," Phys. Rev. E **76**, 016306 (2007).
[22] J. Zhang, A. Oron, and R. P. Behringer, "Novel pattern forming states for Marangoni convection in volatile binary liquids," Phys. Fluids **23**, 072102 (2011).
[23] P. F. Arroiabe, A. Martinez-Urrutia, X. Pena, M. Martinez-Agirre, and M. M. Bou-Ali, "On the thermodiffusion effect in vertical plate heat exchangers," Eur. Phys. J. E **42**, 85 (2019).
[24] N. Grigoreva and V. Nakoryakov, "Exact solution of combined heat- and mass transfer problem during film absorptions," J. Engineering Physics **33(5)**, 1349–1353 (1997).
[25] G. Grossman, "Simultaneous heat and mass transfer in film absorption under laminar flow," Int. J. Heat Mass Transfer **26**, 357–371 (1983).
[26] E. Hofmann and H. C. Kuhlmann, "On the optimum mass transfer of flat absorbing falling films," Int. J. Heat Mass Transf. **55**, 7686–7697 (2012).
[27] K. Hasegawa and Y. Manzaki, "Marangoni fireworks: Atomization dynamics of binary droplets on an oil pool," Phys. Fluids **33**, 034124 (2021).
[28] R. Dandekar, A. Pant, and B. A. Puthenveettil, "Film spreading from a miscible drop on a deep liquid layer," J. Fluid Mech. **829**, 304–327 (2017).
[29] L. Keiser, H. Bense, P. Colinet, J. Bico, and E. Reyssat, "Marangoni bursting: Evaporation-induced emulsification of binary mixtures on a liquid layer," Phys. Rev. Lett. **118**, 074504 (2017).
[30] F. Wodlei, J. Sebilleau, J. Magnaudet, and V. Pimienta, "Marangoni-driven flower-like patterning of an evaporating drop spreading on a liquid substrate," Nature Communications **9**, 820 (2018).
[31] K. Hasegawa and Y. Kishimoto, "Fingering instability of binary droplets on oil pool," Fluids **8** (2023).